
Surface waves on a layered sample at high pressure studied by picosecond acoustics

M2 Acoustics Internship of the Master's in Mechanics at Sorbonne University
conducted from March 4th to July 26th 2024

Xiuyu JIN

Supervised by Simon AYRINHAC

Host Institution : IMPMC

Oral defense : 12/09/24

Updated version : 24/10/24

Contents

1	Surface waves on a layered sample at ambient conditions	4
1.1	General introduction	4
1.2	Surface waves	4
1.3	Rayleigh wave velocity	5
1.3.1	Case of a semi-infinite substrate	5
1.3.2	Case of a layer deposited on a semi-infinite substrate	6
1.4	Experimental technique : picosecond acoustics	7
1.4.1	Time-domain Brillouin scattering	8
1.4.2	Surface imaging	9
1.5	Results	10
1.5.1	Surface waves on various substrates	10
1.5.2	Surface waves on glassy samples	12
	The samples	12
	TDBS measurements	12
	Surface imaging	13
1.6	Conclusion of this section	16
2	Surface waves on a layered sample at high pressure	17
2.1	High pressure experiments	17
2.2	Scholte waves and leaky Rayleigh waves	19
2.3	Results	21
2.3.1	TDBS measurements	21
	In the glass substrate	21
	In the fluid	22
2.3.2	Surface imaging measurements	22
	Velocities of surface waves	22
	Which PTM for future studies ?	25
2.4	General conclusion and perspectives	26

Internship Topic and Implemented Skills

Internship Topic

The internship topic involves studying surface waves on transparent samples using picosecond acoustics techniques [1, 2]. This internship is divided into two parts. The first part focuses on the study of surface waves (Rayleigh and head waves) in transparent samples under normal temperature and pressure conditions, using glass samples coated with a thin aluminum layer. The picosecond acoustics setup allows surface imaging, thereby enabling the visualization of surface waves. The second part involves studying the surface waves of transparent samples under high pressure combining the picosecond acoustics technique with a diamond anvil cell (DAC). The combination of measuring Rayleigh and head waves [3] should provide insights into the elastic properties of the substrate, particularly in determining the velocities of transverse waves, a challenging aspect in picosecond acoustics [4, 5].

List of Implemented Skills

- Measure and visualize surface acoustic waves by picosecond acoustics.
- Acquire an understanding of the instrumentation commonly used in picosecond acoustics, including laser systems, interferometers, and diamond anvil cells (DAC), among others, and master the operational techniques required to conduct experiments with these instruments.
- Master the fundamental principles of picosecond acoustics, including photoacoustic techniques for generating and measuring surface acoustic waves.
- Learn sample preparation techniques, including laser cutting of samples.

Presentation of the Host Organization

The host institute for this internship is the Institut de Minéralogie, de Physique des Matériaux et de Cosmochimie (IMPMC), a collaborative research unit of Sorbonne Université, CNRS, Muséum national d'Histoire naturelle (MNHN), and Institut de recherche pour le développement (IRD). Located at Sorbonne Université in Paris, the IMPMC is multidisciplinary, combining expertise in physics, biology, and mineralogy to explore the structure and behavior of matter and its interactions with microorganisms.

The institute employs about 80 permanent researchers and faculty, alongside around 40 engineers, technicians, and administrative staff. Research at IMPMC spans several areas, including the study of synthetic and natural materials, properties of matter under extreme conditions, and mineral transformations influenced by biological activities.

IMPMC's facilities include advanced equipment for a wide range of scientific investigations, from electron microscopy to spectroscopy. The institute also features a mineral collection, which is a part of its educational and research resources.

The official website of the laboratory is: <https://impmc.sorbonne-universite.fr/>



Figure 1: The official website of the laboratory

Acknowledgments

Simon Ayrinhac^[1], Silvia Boccato^[1], Michel Gauthier^[1], Frédéric Decremps^[1], Marc Morand^[1], Yiuri Garino^[1], Yoann Guarnelli^[1], Paraskevas Parisiadis^[1], Isabelle Roch-Jeune^[2], Tony Valier-Brasier^[3].

[1] Institut de minéralogie, de physique des matériaux et de cosmochimie (IMPMC), Sorbonne Université.

[2] Institut d'Electronique, de Microélectronique et de Nanotechnologie (IEMN), Université de Lille.

[3] Institut Jean le Rond d'Alembert, Sorbonne Université.

Chapter 1

Surface waves on a layered sample at ambient conditions

1.1 General introduction

In picosecond acoustics, generating and detecting shear waves in isotropic materials is a major challenge [6]. In anisotropic materials, such as silicon [7] or MgO [2], the focalisation of the pump beam produces diffraction and permits easily to generate shear waves. However, in isotropic materials, when photoelastic generation is based on thermoelastic effects, shear acoustic waves are not excited at all in a single heated point in the material volume. Due to the isotropy of thermal expansion, thermal expansion proceeds equivalently along all possible directions from the heated point, and the particle displacement remains spherically symmetric, and no shear deformation occurs. Therefore, shear acoustic waves are not naturally generated in homogeneous isotropic materials, and overcoming this limitation requires breaking the material's symmetry.

Another approach is to generate waves which combine longitudinal and shear properties (generally surface waves) to indirectly determine the shear velocity [8, 3, 9, 10]). This is called "inversion technique" (see Ref.[11]). For example, Mante *et al* (2008) [8] have used a nanostructured aluminum film to excite and detect high-frequency acoustic waves. The vibration of the nanocubes, in the limiting case where they are infinitely spaced, gives a velocity equals to the Rayleigh wave velocity. Combining this with the determination of the longitudinal velocity from time Brillouin-scattering and the knowledge of refractive index, enable the determination of the transverse sound velocity in submicron films.

Xu *et al* (2013) [9] refined the method, measuring the Brillouin frequency at various incidence to obtain an absolute value of the longitudinal velocity, and measuring Rayleigh wave velocity by Phonon imaging and obtaining dispersion curve. Combined with a determination of the density, from the amplitude decay of the echoes and evaluation of the impedance mismatch, they obtain a complete characterization of the thin film under study with the minimum of assumptions.

In this study, we plan to obtain the longitudinal velocity and shear velocity by measuring the velocities of Rayleigh and lateral waves by the picosecond acoustic technique. In the case where the sample is transparent, an absorbing layer must be deposited on top, which affects obviously the propagation of waves in a proportion that must be quantified.

1.2 Surface waves

Using picosecond acoustics, we can excite surface acoustic waves to assess the thickness of thin films and the elastic constants of substrates. The types of surface acoustic waves excited include Rayleigh

waves and lateral Waves (sometimes called head waves).

Rayleigh waves are a type of surface acoustic wave that travels along the surface of solids. They are characterized by their proximity to the surface and include both longitudinal and transverse component motions. The amplitude of these waves decreases exponentially with distance from the surface, and there is a phase difference between the component motions. In isotropic solids, Rayleigh waves cause surface particles to move in elliptical paths within planes perpendicular to the surface and parallel to the direction of wave propagation, with the major axis of the ellipse being vertical. The velocity of the Rayleigh waves is slightly less than that of shear waves, dependent on the elastic constants of the material (see Section 1.3).

Lateral waves, equivalent to head waves at the free surface, are another type of surface acoustic wave, typically travel faster than Rayleigh waves. They propagate at the same velocity as longitudinal waves travelling parallel to the free surface and share the same geometrical shape as the boundary between the different media (see Fig. 1.1 using a two-dimensional finite-difference model [12]).

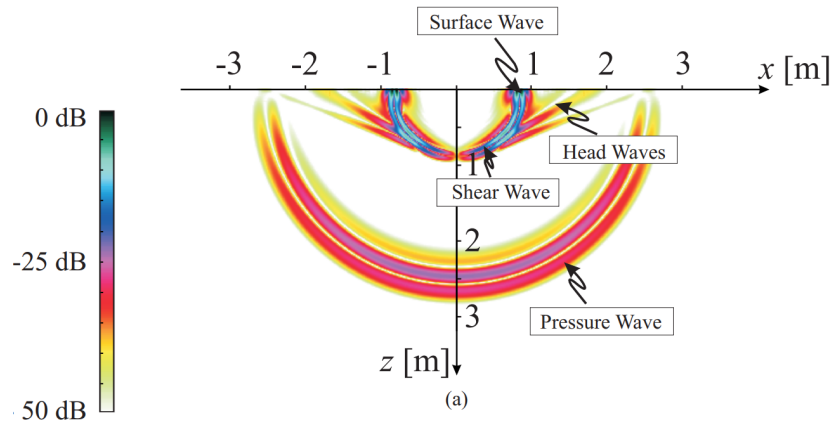


Figure 1.1: Simulated waves propagating in a semi-infinite and isotropic solid (at the bottom) bounded by a free surface (at the top), and excited by a point source located in $(x,z)=(0,0)$ [12].

1.3 Rayleigh wave velocity

1.3.1 Case of a semi-infinite substrate

To calculate the Rayleigh wave velocity, the well-named Rayleigh equation is used, but Viktorov's approximation is often employed for simplicity.

The analytical Rayleigh equation is satisfied by v_R [13] if

$$16 \left(1 - \frac{v_R^2}{v_L^2}\right) \left(1 - \frac{v_R^2}{v_T^2}\right) - \left(2 - \frac{v_R^2}{v_T^2}\right)^4 = 0, \quad (1.1)$$

where v_L and v_T are respectively the longitudinal and transverse (shear) velocity in the substrate.

The Viktorov equation [13], which gives a good approximation of v_R , is frequently used :

$$\frac{v_R}{v_T} = \frac{0.718 - (v_T/v_L)^2}{0.75 - (v_T/v_L)^2}. \quad (1.2)$$

We can see in Table 1.1 that the Viktorov's equation give different (10-20 m/s) than the exact solution. In the following, we will refer always to the exact solution.

Material	Nature	ρ (kg/m ³)	v_L (m/s)	v_T (m/s)	v_R (Viktorov) (m/s)	v_R (exact) (m/s)
soda-lime glass [14]	amorphous (*)	2490	5840	3460	3182.5	3169.4
borosilicate glass [15]	amorphous (*)	2230	6050	3690	3377.1	3364.0
aluminum (A1050) [16]	polycrystalline	2700	6470	3150	2953.5	2942.8
ZnO [17]	polycrystalline	5700	6000	2831	2659.2	2649.9
Si [17]	polycrystalline	2331	8945	5341	4906.6	4886.5
SiO ₂ [18]	amorphous	2200	5970	3776	3430.7	3417.9

Table 1.1: Elastic properties of standard isotropic materials from literature data. (*) These glasses are essentially rich in silica SiO₂ (70-80%), but borosilicate glass have a composition more rich in boron trioxide B₂O₃, whereas soda-lime glass have more sodium oxide Na₂O.

1.3.2 Case of a layer deposited on a semi-infinite substrate

The deposited layer on the substrate affects obviously the propagation of the Rayleigh wave, depending on its thickness and nature. A complete modelisation was proposed by Farnell *et al* [17].

In the experiment, both the layer and substrate materials are non-piezoelectric and isotropic. According to Farnell et al. (1972)[17], the boundary condition equations for isotropic media can be divided into two distinct groups when electrical conditions are disregarded. One group involves roots a , 1, and 2, which pertain to transverse displacement components. The other group involves roots 5, 6, 7, 8, c , and d , relating to displacements in the sagittal plane. This leads to two independent types of solutions:

- "Love modes" for transverse displacements only and
- "Rayleigh-like modes" or simply "Rayleigh modes" for sagittal-plane displacements, echoing the Rayleigh waves on unlayered free surfaces.

We focus on Rayleigh modes, and therefore, only the six mechanical conditions detailed in section II.C of Farnell et al.'s paper (1972) are relevant. These conditions involve six constants $C^{(q)}$, labeled 5, 6, 7, 8 for the layer, and c, d for the substrate.

Noting k the wave number, and v the velocity to be determined, the displacement for the layer is

$$\hat{u}_j(x_1, x_3, t) = \left(C^{(5)} \alpha_j^{(5)} e^{ikb^{(5)}x_3} + C^{(6)} \alpha_j^{(6)} e^{ikb^{(6)}x_3} + C^{(7)} \alpha_j^{(7)} e^{ikb^{(7)}x_3} + C^{(8)} \alpha_j^{(8)} e^{ikb^{(8)}x_3} \right) e^{ik(x_1-vt)}, \quad (1.3)$$

whereas the displacement for the substrate is

$$u_j(x_1, x_3, t) = \left(C^{(c)} \alpha_j^{(c)} e^{ikb^{(c)}x_3} + C^{(d)} \alpha_j^{(d)} e^{ikb^{(d)}x_3} \right) e^{ik(x_1-vt)}. \quad (1.4)$$

Then Eq. (1.3) and (1.4) are used in combination with the mechanical sagittal boundary conditions labelled (7)-(12) and leads to the equation (see Eq.(18) in [17] ¹)

$$\begin{vmatrix} b^{(5)} & -1 & -b^{(5)} & -1 & -b^{(c)} & 1 \\ -1 & -b^{(6)} & -1 & b^{(6)} & 1 & b^{(d)} \\ (1-b^{(5)2}) & 2b^{(6)} & (1-b^{(5)2}) & -2b^{(6)} & -r(1-b^{(c)2}) & -2rb^{(d)} \\ 2b^{(5)} & -(1-b^{(5)2}) & -2b^{(5)} & -(1-b^{(5)2}) & -2rb^{(c)} & r(1-b^{(c)2}) \\ (1-b^{(5)2})e^{ib^{(5)}kh} & 2b^{(6)}e^{ib^{(6)}kh} & (1-b^{(5)2})e^{-ib^{(5)}kh} & -2b^{(6)}e^{-ib^{(6)}kh} & 0 & 0 \\ 2b^{(5)}e^{ib^{(5)}kh} & -(1-b^{(5)2})e^{ib^{(6)}kh} & -2b^{(5)}e^{-ib^{(5)}kh} & -(1-b^{(5)2})e^{-ib^{(6)}kh} & 0 & 0 \end{vmatrix} = 0 \quad (1.5)$$

¹An error was reported in the paper, in the fifth line and fourth column $2b^{(5)}e^{ib^{(6)}kh}$ should be replaced by $2b^{(6)}e^{ib^{(6)}kh}$.

where h is the thickness of the layer, $b^{(c)} = -i\sqrt{1 - v/v_T^2}$, $b^{(d)} = -i\sqrt{1 - v/v_L^2}$ for the substrate with v_L and v_T are respectively its longitudinal and longitudinal velocity ; $b^{(5)} = i\sqrt{1 - v/v_{LT}^2}$, $b^{(6)} = i\sqrt{1 - v/v_{lL}^2}$ for the layer, with v_{lL} and v_{lT} are respectively its longitudinal and longitudinal velocity;

The influence of the material layer on the phase velocity of Rayleigh waves is explored for two distinct cases, as illustrated in Figure 1.2: (a) ZnO/Si (polycrystalline), a scenario previously analyzed by Farnell [17], and (b) Al(1050)/soda-lime glass, which is the focus of our current study. For the ZnO/Si case, the relevant values are provided in Table 1.1.

The relationship between the phase velocity and group velocity $v_g(kh)$ for Rayleigh waves is further elucidated through the equation given by Farnell (see Eq. (27) in Ref. [17]):

$$v_g = v_\phi(kh) + kh \frac{dv_\phi(kh)}{dkh}. \quad (1.6)$$

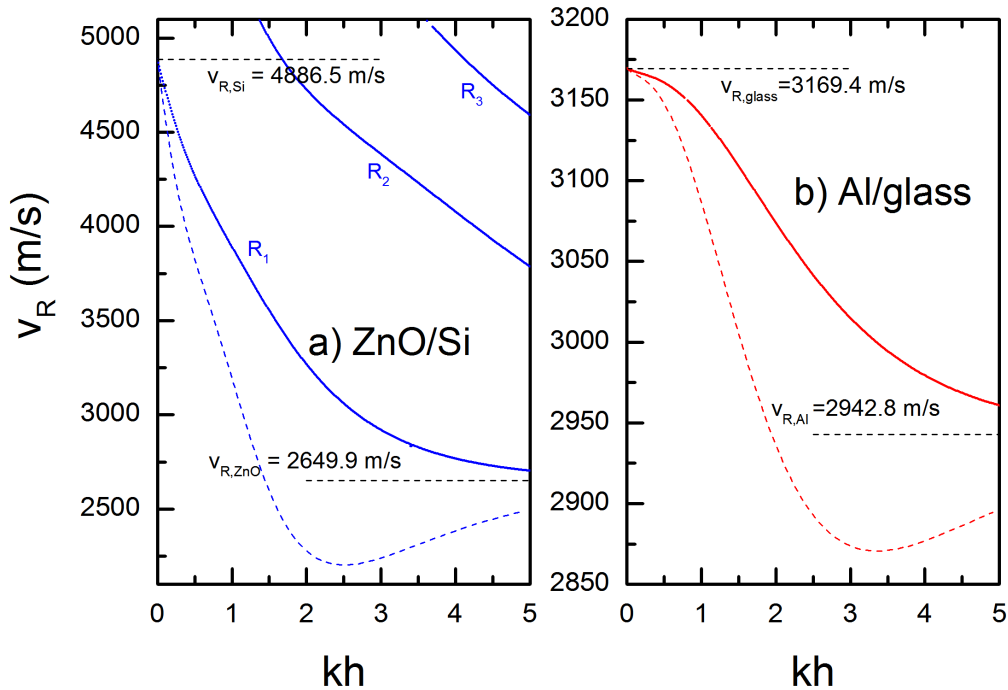


Figure 1.2: Phase velocity (solid lines) and group velocity (dashed lines) of the Rayleigh wave v_R as a function of kh for two cases (calculated from Eq. 1.5): (a) polycrystalline ZnO/Si (with the first three Rayleigh modes labelled R_1 , R_2 and R_3) ; (b) Al/glass.

1.4 Experimental technique : picosecond acoustics

Picosecond acoustics [1] is an advanced nondestructive pump-probe technique used within ultrafast optical methods to explore the mechanical and thermal properties of materials, particularly useful for thin-film samples. This method uses a Ti:Sapphire laser, with a wavelength tunable now operating at $\lambda_0=960$ nm and with a repetition rate of 12.494 ns. In our set-up, the laser generates ultrashort pulses of 100 fs, split into pump and probe beams focused on opposite surfaces of the sample (see Fig 1.3). The absorption of the pump optical pulse at the sample surface induces a temperature

increase, causing thermal expansion and subsequent generation of acoustic strain fields. The probe beam pass four times through a mechanical delay line (length 1 m) which allows to modify the time delay between pump and probe up to 13.33 ns.

As these fields propagate, they influence the sample's optical reflectivity due to the photo-elastic effect and surface displacement. This change in reflectivity, captured through interferometry, is analyzed using a stabilized Michelson interferometer, which facilitates the precise determination of reflectivity changes. An acousto-optic modulator (AOM) allows to measure very weak signals by modulation of the pump at 1 MHz and then demodulation of the photodiode signal by a lock-in amplifier. Aided by high-resolution microscopy with a Mitutoyo 20X NIR objective (NA=0.4, $f=10$ mm), both beams are sharply focused (the theoretical beam spot diameter is $d = 2\lambda_0/\pi\text{NA} = 1.53 \mu\text{m}$), enabling imaging of the sample surface with the help of a piezoelectric X-Y stage. The piezoelectric stage can explore areas up to $100 \times 100 \mu\text{m}^2$.

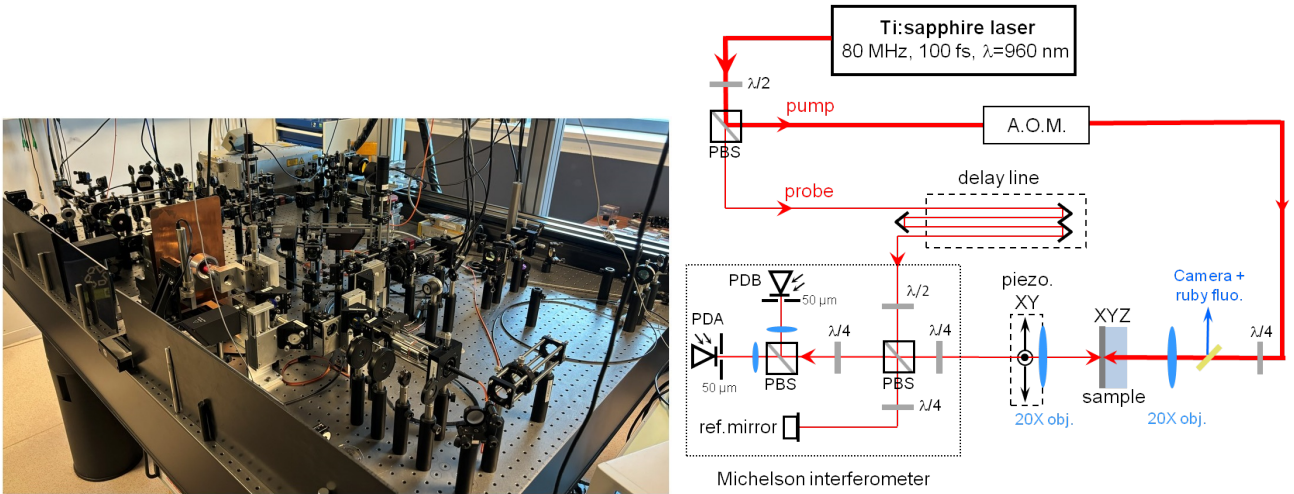


Figure 1.3: **(left)** A photograph of the set-up (at IMPMC). **(right)** Schematic view of the set-up. PBS : polarizing beamsplitter ; AOM : acousto-optic modulator ; $\lambda/2$: half-wave plate ; $\lambda/4$: quarter-wave plate ; PDA/PDB : photodiodes A and B ; XY(Z) : translation stages ; 20X obj. : 20X near infrared objectives.

1.4.1 Time-domain Brillouin scattering

The transparency of the substrate allows the observation in the signal of typical "Brillouin oscillations". It appears in the relative variations of refractive index $\Delta r/r$ induced by the propagating wave as damped sinusoidal oscillations, when pump and probe beams are colinear. The oscillations arise from interferences between the probe light reflected by the static interfaces and the moving acoustic pulse [19]. This technique is often called time-domain Brillouin scattering (TDBS).

The frequency of Brillouin oscillations, denoted as f_B , is determined by

$$f_B = \frac{2nv_L}{\lambda_0}, \quad (1.7)$$

where n is the refractive index of the glass substrate at λ_0 , and v_L represents the adiabatic longitudinal sound velocity (or compressional in the case of fluid). During their propagation in the sample, these Brillouin oscillations are attenuated. The Brillouin oscillations appears as damped sinusoidal oscillations, and the relative variations of refractive index $\Delta r/r$ can be described by

$$\frac{\Delta r}{r}(t) = A \sin \left(2\pi \frac{t}{T} + \phi \right) e^{-\alpha v_L t}, \quad (1.8)$$

where A is an amplitude coefficient, ϕ is the phase at the origin, T is the period of the oscillations simply related to the frequency f_B by $f_B = 1/T$ and α is an attenuation coefficient. This coefficient includes acoustic damping at the frequency f_B (geometrical and intrinsic), optical damping at the laser beam wavelength λ_0 (generally negligible in glasses), the focusing effect due to microscope objective, and the geometrical damping due to diffraction of the acoustic wave [20].

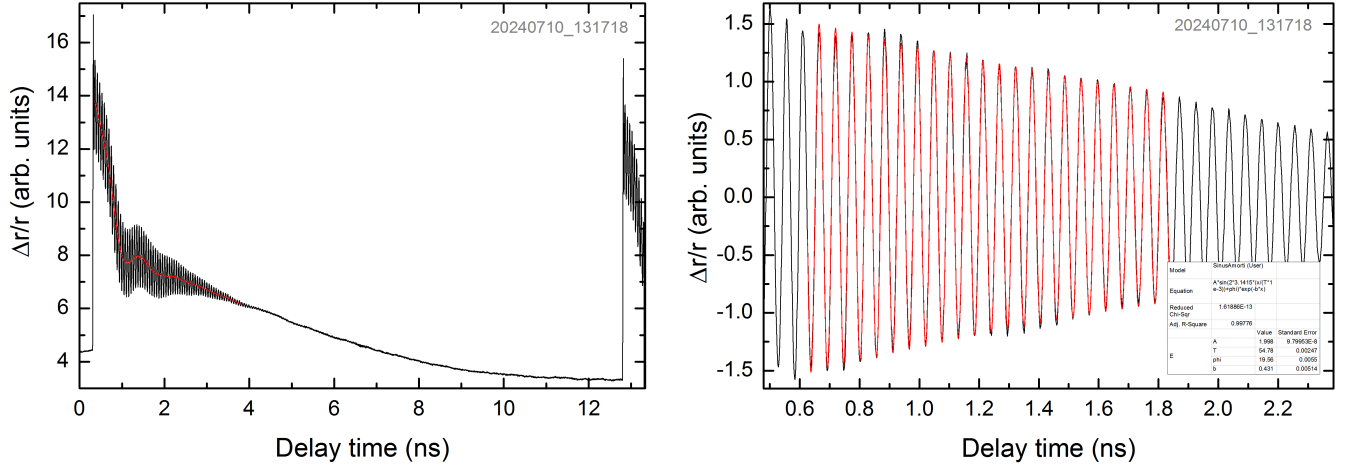


Figure 1.4: **(left)** Typical signal (average of 369 scans) of 100 nm Al layer on microscope slide glass when pump and probe are collinear, in transmission configuration (pump beam on air/Al side, and probe beam on Al/glass side) and in interferometric mode. The smooth decrease of the signal is due to thermal relaxation. **(right)** Fitting of the Brillouin oscillations by Eq. (1.8), after subtracting the background by a Savitzky-Golay algorithm (500 points, polynomial order 2, see red line in the left figure). It gives $T = 54.789 \pm 0.002$ ps, and $\alpha v_L = 0.431 \pm 0.005$ ps⁻¹.

1.4.2 Surface imaging

The probe beam pass through an objective mounted on a piezoelectric device which allows to perform surface imaging of the sample, over an area of $100 \times 100 \mu\text{m}^2$. The simultaneous use of the delay line makes it possible to record the evolution of the waves arriving at the surface (bulk waves or pure surface waves) as a function of time, what can be called a "movie".

The propagation of surface waves on the sample's surface, which have the shape of circles centred on the spatial coincidence of the pump/probe beams for isotropic samples or have more complex shapes for anisotropic solids, can be tracked using surface imaging. For these surface waves, the radius of the circles increases linearly with the delay time, as shown in Fig.(1.5). We plot the measured data as a graph of the radius as a function of the delay time, according to the equation $R(t) = vt$. The surface wave velocity v is simply the slope of the $R(t)$ graph, obtained from a linear fit.

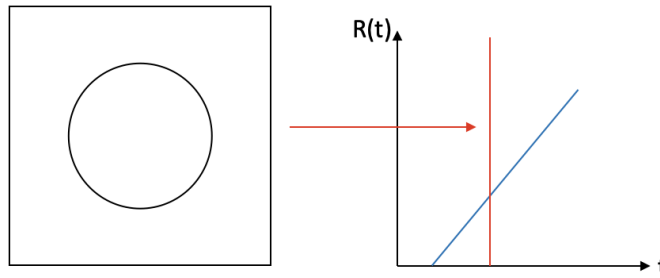


Figure 1.5: **(Left)** Schematic diagram of surface imaging, after a certain delay time, representing a circular ripple due to a surface wave. **(Right)** Schematic representation of the variation of the radius of surface waves over time after processing the surface imaging (blue line). TDBS measurements are performed at $R=0$.

1.5 Results

1.5.1 Surface waves on various substrates

On a preliminary study, to illustrate the capabilities of the technique, we obtained surface waves imaging on various substrates [21], as shown in Fig. (1.6). In the experiment, the samples we selected consist of aluminum layers, each with a thickness of 150 nm, deposited on various substrates (anisotropic or not) including quartz, LiF, sapphire, diamond, fused silica (SiO_2), and finally an iron (Fe) deposited on glass.

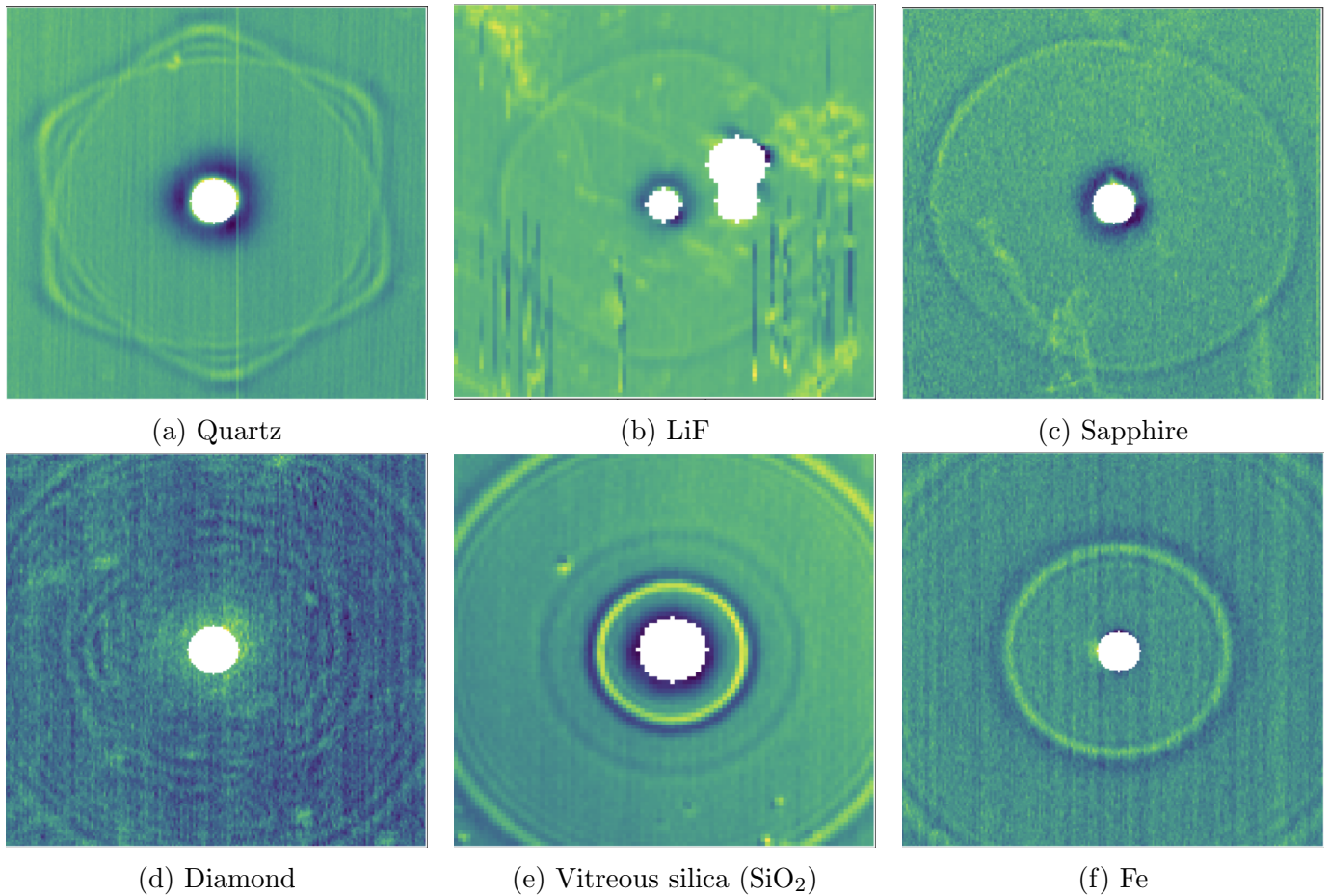


Figure 1.6: Surface waves on various substrates, visualised in the xy plane (area $100 \times 100 \mu\text{m}^2$). Note: white areas represent removed thermal signal or static reflectivity defects, which are very intense with respect to waves and are not of interest in this study.

From Fig.(1.6), we observe diverse surface wave patterns on different substrates. This variation is due to the distinct crystal structures and anisotropic characteristics of these substrates, which influence the shape of the surface wave patterns, allowing us to observe different acoustic wave features :

- Quartz, as a hexagonal crystal system, exhibits significant anisotropy, with its surface waves forming a six-pointed star pattern as shown in Fig. (1.6a).
- LiF is a cubic crystal system, characterized by anisotropy, and displays a slightly distorted circular pattern in surface waves as seen in Fig. 1.6b.
- Sapphire, a trigonal crystal system, shows pronounced anisotropy, with its surface waves presenting an elliptical pattern in Fig. 1.6c.
- Diamond, an anisotropic cubic crystal, and its high hardness contribute to a very unique surface wave pattern. Due to the large difference of impedance between aluminum and diamond, the layer of aluminum vibrates (phenomenon of "ringing" [22]) and produces multiple fine ripples (see Fig. 1.6d).
- Silica (amorphous SiO_2 , UVFS grade) is a glass and thus elastically isotropic, and in Fig. 1.6e it is clear that the surface waves present a circular pattern. The Rayleigh velocity was determined

to be $v_R = 3219 \pm 6$ m/s ($\nu_{max}=0.39$ GHz), and the head wave velocity $v_H = 5802 \pm 51$ m/s ($\nu_{max}=0.67$ GHz).

- A layer of polycrystalline Fe (250 nm evaporated on glass), containing a large number of randomly oriented grains, appears isotropic at the macro level, and in Fig. 1.6f, we can observe that the surface waves also present a circular pattern. The multiple ripples are likely due to dispersion. The Rayleigh velocity was determined to be $v_R = 2896 \pm 34$ m/s, at $kh = 0.174$.

1.5.2 Surface waves on glassy samples

The samples

The samples consist of a thin aluminum layer deposited on standard glasses : microscope slides and cover slips, with characteristics indicated in the Table. 1.2 (see Fig. 1.7, left). This is test samples which have been coated with nice layers of aluminium, and they are readily available in our laboratory. At the beginning of our work, the exact type of glass involved was unknown. To enhance the adhesion of the layer, a preliminary etching with argon plasma was conducted, followed by deposition through vacuum evaporation in the clean room at IEMN [23] (thanks to Silvia Boccatto from IMPMC, and Isabelle Roch-Jeune, from Centrale de Micro et Nanofabrication, Institut d’Electronique de Microélectronique et de Nanotechnologie, UMR CNRS 8520, Villeneuve d’Ascq, France). The nominal thicknesses of the aluminum layers are 50, 100, 150, and 200 nm. Profilometry gave respectively 33-63², 99, 150 and 202 nm. The properties of the deposited aluminum are assumed identical to the properties of the bulk polycrystalline aluminum. The same aluminum layer was deposited on the two kind of glasses, but different layers are deposited on different slides. In this work we assume that the 4 cover slips (and the 4 microscope slides) are from the same batch and have an identical composition.

Substrate material	e (mm)	l (mm)	L (mm)	m (g)	ρ (kg/m ³)
microscope slide glass	1.08 ± 0.02	25.52 ± 0.04	75.76 ± 0.06	5.19 ± 0.01	2490 ± 50
cover slip glass	0.150 ± 0.005	22.46 ± 0.04	22.46 ± 0.04	0.168 ± 0.004	2210 ± 90

Table 1.2: Typical properties of glass substrates : e is thickness, l width, L length, m mass and ρ the density simply determined by $\rho = m/elL$.

TDBS measurements

We conducted Brillouin oscillation analysis on both types of glass, using damped sinusoidal wave fitting, and obtained the results shown in Fig 1.7 (right). According to this figure, we found significant differences in the nv_L between the two types of glasses. This suggests that the elastic properties of the two kinds of glasses are different. We performed statistical analysis to obtain the mean values shown in Fig.(1.7) and reported in Table 1.3 (p. 16).

²The profilometer is not precise enough for 50 nm, hence only a trend is provided.

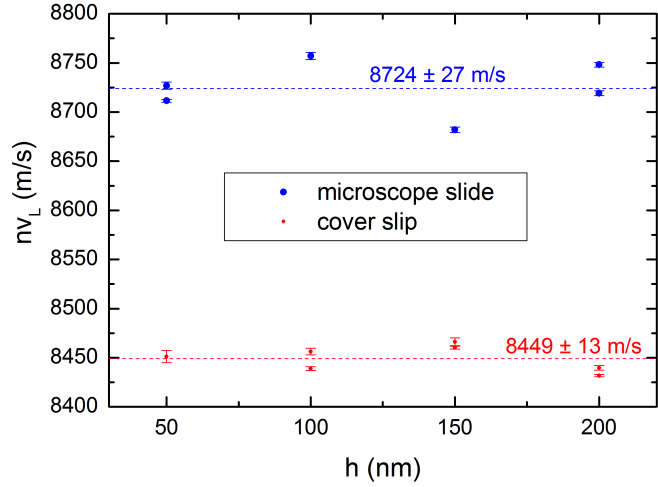


Figure 1.7: **(left)** A microscope slide (top) and a cover slip (bottom) [Credit image : Wikipedia]. **(right)** Comparison of nv_L between the two types of glasses obtained by Brillouin oscillations. The error bars of each point are derived from the fits. The statistical value indicated on the graph is the arithmetic mean (no weighted), and the error bar is the corrected sample standard deviation.

Surface imaging

For each sample, surface imaging as a function of time was performed.

To enhance the signal-to-noise ratio, we integrated circular patterns and collected data on the changing radius over time. This process yielded the radius R as a function of time t , as shown in Fig. 1.8 for the sample with 150 nm aluminum layer on microscope slide glass. In the three images in Fig. 1.8 (upper part), the head wave is highlighted by orange arrow (top panel) or circle (bottom panel), while the Rayleigh wave is highlighted by red arrow (top panel) or circle (bottom panel). The white areas, which originally contained thermal signals, were removed as they were of no interest.

Since the relationship between the surface wave radius and time is linear, we were able to determine the slope to calculate the velocities of the head wave and Rayleigh wave. The Rayleigh wave velocity was determined to be $v_R = 3164.3 \pm 1.2$ m/s, and the head wave velocity was $v_H = 5782 \pm 8$ m/s.

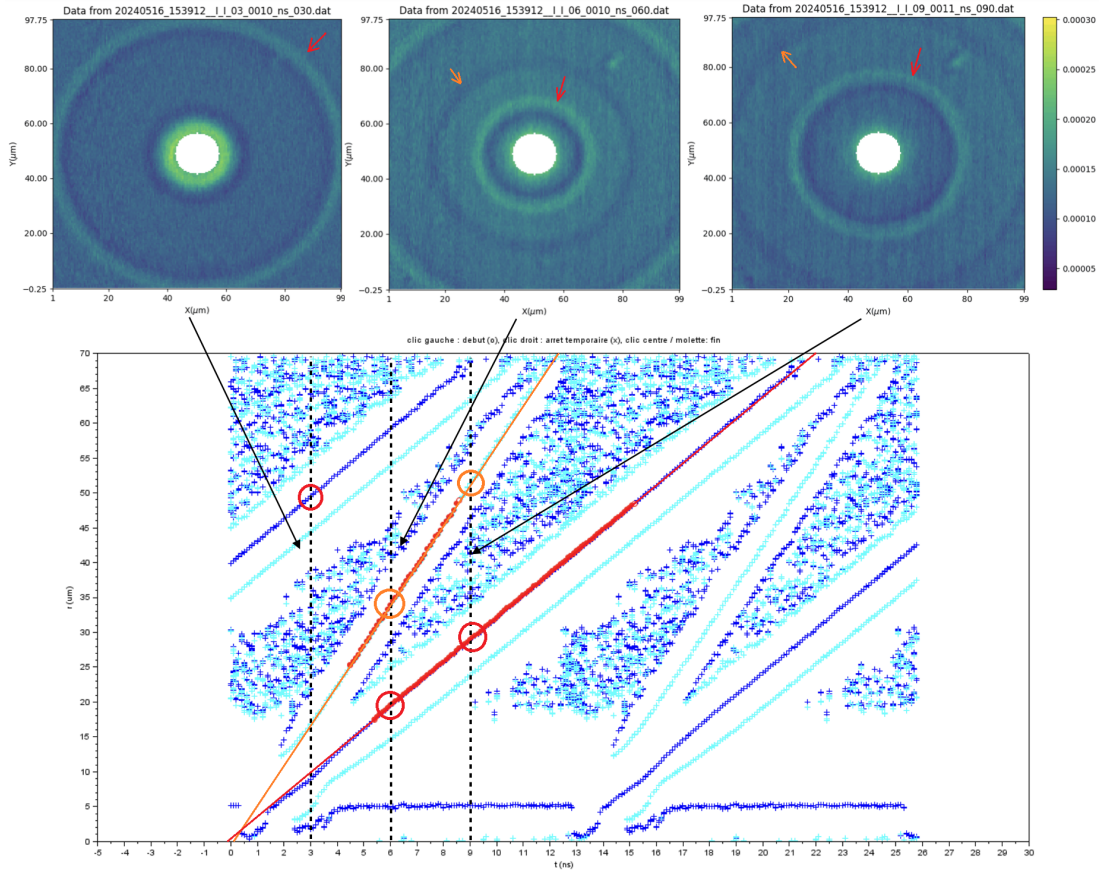


Figure 1.8: **(Above)** Three pictures from surface imaging on 150 nm aluminum layer on microscope slide glass, at different delay times, showing multiple circular patterns due to propagating surface waves. From each picture, profiles are generated by integrating the circular patterns. **(Below)** Radius as a function of time, showing only maxima (dark blue points) and minima (light blue points). Surface waves appear as lines, and velocities v are obtained from a linear fit such as $R(t) = v(t - t_0)$.

Using this method, we obtained the experimentally measured v_R and v_H values for glass substrate covered by aluminum layers with nominal thicknesses of 50 nm, 100 nm, 150 nm, and 200 nm.

Based on the theory discussed in Section 4.4, we plotted the theoretical curves of v_R versus kh for the aluminum-coated microscope slide glasses and cover slip glasses. The determination of the k value is challenging because surface waves are wave packets, which complicates their spectral analysis compared to purely monochromatic waves. Where possible, we processed the experimental data using a Fourier transform for time-frequency analysis. The peak position of the Fourier transform was approximated as the mean frequency of the wave packet, ν_{max} , which helps in estimating the most significant frequency component within the polychromatic spectrum.

In the case where surface imaging was done, the frequency ν_{max} is deduced from the gap between the maxima and minima linear curves. If we assume a simple bipolar shape $f(t)$ for the Rayleigh wave where the two maxima are separated by a delay τ , the Fourier transform (FT) is $F(\nu)$



$$f(t) = Ate^{-\frac{2t^2}{\tau^2}} \xrightarrow{\text{FT}} F(\nu) = A'\nu e^{-\frac{1}{2}\pi^2\tau^2\nu^2}, \quad (1.9)$$

and then $\nu_{max} = \frac{1}{\pi\tau}$. Generally $\tau \simeq 1.5$ ns, so $\nu_{max} \simeq 0.2$ GHz.

Using this frequency in the equation $k = \frac{2\pi}{\lambda_{ac,mean}} = \frac{2\pi\nu_{max}}{v_R}$, we calculated the corresponding kh values, which allowed us to plot the theoretical curves of v_R versus kh for the microscope slide and coverslip, as shown in Fig1.9(a). Astonishingly, the kh maximum depends strongly of the sample : for microscope slide glass is 0.075 and for the cover slip glass it is 0.15. It could be due to the different thicknesses of the glass's substrates, 1 mm and 150 μm . The focalisation of the pump beam (and also the probe beam) is altered by the thickness of the glass, a thick glass involving a bad focalisation.

In Fig. 1.9(a), the solid line represents the phase velocity, while the dashed line represents the group velocity. For our data analysis, we primarily relied on the group velocity, as it is more suitable for analyzing wave packets with a broad frequency range. Phase velocity is typically applicable to monochromatic waves, but our experiment deals with wave packets. The mean frequency of the wave packet is influenced by the lateral size of the laser spot, making group velocity a more accurate representation of the wave packet's propagation characteristics.

In our experiments, we used kh values of 0.2 or less.

At such low kh values, it is difficult to distinguish between different samples because the Rayleigh wave velocity becomes independent of the layer thickness. This confirms that, regardless of the thin layer's thickness, we can measure the Rayleigh velocity of the substrate. Concerning the head waves, they are considered independant of the layer thickness, and a statistical analysis can be performed (see Fig. 1.9(b)).

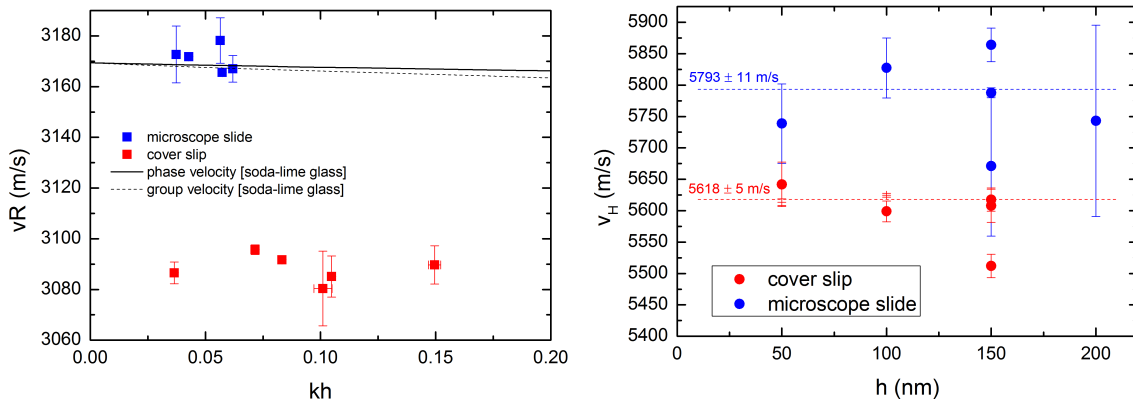


Figure 1.9: **(a)** Velocities of the Rayleigh wave as a function of kh for two types of glass substrates. The calculated phase velocity and group velocity for soda-lime glass are shown for comparison. **(b)** Head wave velocities for the two types of glasses. The mean of the data is the weighted arithmetic mean, and the error bar is the standard error of the mean, both with instrumental weighting.

In the previous section, we showed that the Rayleigh wave is not slowed down by the aluminum layer. The bulk properties of the substrate (here glass) are therefore determined from the surface waves.

The surface waves permit to deduce v_L and v_T . As shown in Table 1.3, the elastic properties of the two standard glasses are slightly different. Velocities of the microscope slide glass are significantly higher than the velocities of the cover slip glass (which will be used in our experiments at high pressure). The same trend is observed by the measuring method of Brillouin oscillations (see Fig.1.7).

The properties of the microscope slide glass are very similar to the properties of soda-lime glass, as reported in Table 1.1. About the cover slip glass, the density corresponds to that of borosilicate glass, but not the velocities.

The frequency f_B of the oscillations (Eq. 1.7) allows us to determine the refractive index of the glass at $\lambda_0 = 960$ nm. The refractive index, as searched in the Refractive Info database, corresponds among many others to "BK7"³ (crown borosilicate, $n=1.5081$) or "Soda lime glass"⁴ ($n = 1.514$).

The determination of the transverse velocity in the studied slides agrees very well with the known values in such kind of glasses.

Substrate material	exp.			calc.		exp.		calc.
	ρ (kg/m ³)	v_H (m/s)	v_R (m/s)	v_L (m/s)	v_T (m/s)	f_B (GHz)	nv_L (m/s)	$n(\lambda_0)$
microscope slide glass	2490	5793	3167	5793	3462	18.18	8724	1.506
cover slip glass	2210	5618	3092	5618	3244	17.60	8449	1.504

Table 1.3: Some properties of glasses used as substrate samples include both measured (denoted as ‘exp.’) and calculated (‘calc.’) values. The longitudinal velocity v_L is determined from the velocity of the head wave v_H , and the shear velocity v_T is calculated from v_R and v_L using a numerical resolution of Eq.1.1. Additionally, the product of refractive index $n(\lambda_0)$ by v_L is determined from Brillouin oscillations by Eq. 1.7.

1.6 Conclusion of this section

We have demonstrated that, in our set-up configuration, for a thin layer of aluminum below 200 nm, the velocity of the Rayleigh wave on the layered glass substrate is equivalent to the velocity of the Rayleigh wave of the substrate only. This indicates that, in this scenario, the Rayleigh wave velocity depends solely on the properties of the substrate. Consequently, the surface wave velocities allow us to measure the bulk velocities and determine the shear velocity by combining v_R and v_H .

Additionally, we have shown that the elastic properties of the two glasses used as samples are slightly different and have been identified as distinct types of soda-lime glass. However, it is impossible to measure the elastic properties and thickness of the thin aluminum layer using this method. This limitation is significant, as the properties of thin layers can differ from those of bulk material, potentially influenced by factors such as the deposition method.

³<https://refractiveindex.info/?shelf=glass&book=BK7&page=SCHOTT>

⁴<https://refractiveindex.info/?shelf=glass&book=soda-lime&page=Rubin-clear>

Chapter 2

Surface waves on a layered sample at high pressure

In this chapter, velocities of surface waves were measured on a layered sample Al/glass submitted to high pressure. To perform the experiments, a sample was loaded in a specific device called a diamond anvil cell (DAC). This apparatus enables the application of high pressures, allowing us to investigate how surface wave velocities change under such conditions.

2.1 High pressure experiments

The diamond anvil cell (DAC) is currently the only experimental apparatus that can routinely generate static pressures exceeding 300 GPa, 1 GPa representing 10 000 atmospheres ! Diamonds are chosen for generating such extreme pressures because they are the hardest known material and are transparent to photons across a wide energy range. This characteristic allows diamonds to exert tremendous pressure on a very small surface area. A moderate pressure, controlled by the user, is applied to the external part of the diamond (around 100 bar) through a gas-filled membrane, and then, by reducing the surfaces, the pressure at the diamond's culet allows the gasket to be strongly compressed. The maximum pressure achievable by this membrane is about 150 bars. The sample chamber is drilled into a metallic gasket located between the two opposing diamonds. To ensure hydrostatic pressure, the sample chamber is filled by a pressure-transmitting medium (PTM), generally transparent soft fluid or gas. The PTM is very important to reduce large pressure gradients in the sample. The pressure on the sample increases due to the reduction in the volume of the sample chamber. Conversely, when the pressure decreases, the mechanism involved is typically due to leakage of the PTM between the gasket and the diamonds.

Below, Fig. 2.1 provides a schematic diagram, offering a visual representation of the setup.

The DAC employs diamonds with a culet diameter measuring 600 μm and utilizes a rhenium gasket. The initial thickness of the gasket was 285 μm , and it was indented to 182-185 μm , exerting on diamond a maximum membrane pressure of $P_m = 35$ bars followed by material removal by laser drilling. The sample chamber is drilled using a laser drilling system to feature a perfectly circular hole with a diameter of 300 μm . We use silicone oil (47 V 20, a polydimethylsiloxane (PDMS) oil, from Rhodorsil manufacturer) as the pressure transmitting medium (PTM). This PTM was chosen for its availability in the laboratory, and its ease of use to fill the sample chamber. The choice of the PTM is crucial in high-pressure techniques, as we will see later.

The sample used for the experiment consists of a 150 μm thick cover slip coated with a thin layer of aluminum, nominally 100 nm thick. The set-up is in configuration transmission (pump and probe beams are in opposite sides of the sample), the aluminum layer is thick enough to be non-transparent

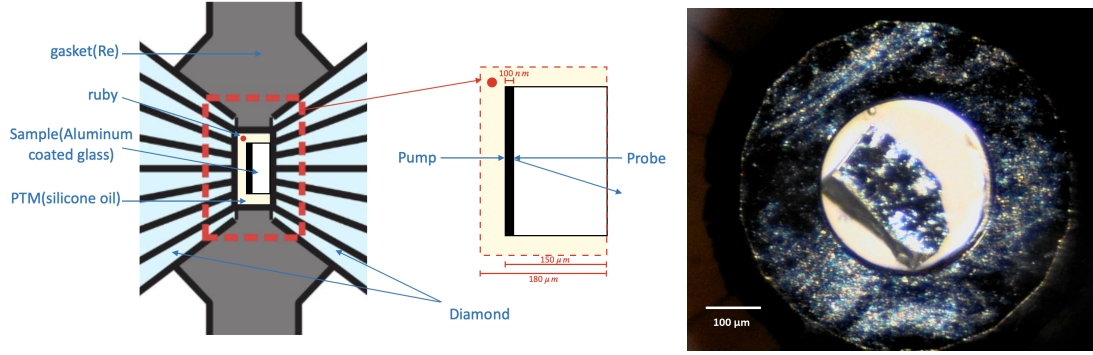


Figure 2.1: **(left)** Schematic view of the sample (Al(100 nm) deposited on cover slip glass 150µm thick) inside the DAC. Here, the probe beam is shown probing the Al/glass side, but the DAC can be rotated to probe the Al/oil side. **(right)** Binocular view of the sample inside the DAC, before oil loading. The outer and largest circle represents the indentation of the diamond culet on the gasket, and the inner circle is the hole drilled in the rhenium gasket. The small sphere at the upper left is the ruby.

for the pump beam. In addition, the residual light from the pump is removed by spatial filtering. The glass substrate was cut by hand, and then a piece was selected to match the size of the chamber hole (see Fig. 2.1, right). This procedure can increase the number of defects on the aluminum layer, which decreases the size of the "clean" zone where measurements can be done. Indeed, interferometric measurements and their stabilization are very sensitive to defects. During the data analysis, it is possible to apply a "mask" to the disturbed zones, as illustrated in Fig. 2.2.

Pressure measurement within the DAC is carried out using the ruby fluorescence technique. This method involves observing the shift in fluorescence emitted by a ruby. The shift in the wavelength of this fluorescence is directly proportional to the pressure applied [24]. For accurate measurements, it is essential to determine the wavelength at ambient conditions, $\lambda_0 = \lambda_{R_1}(P = 0)$, which represents the fluorescence of the ruby under ambient pressure conditions. The raw pressure measurements were adjusted by -0.2 GPa. In this work, we use two rubies to measure the pressure inside the DAC, but only one was used for the analysis of data.

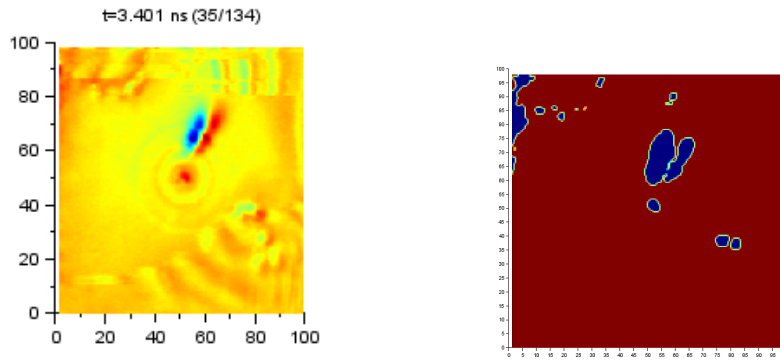


Figure 2.2: **(left)** Surface imaging obtained at 4 GPa on the Al/glass side, at a delay time of 3.401 ns. The color scale reflects the signal intensity. The wave patterns are due to inefficient stabilization of the interferometer, while the blue/red zone represents a static defect (a zone of high or low optical reflectivity). The horizontal and vertical scales are in µm. **(right)** This picture shows the "mask" applied to remove the defects; blue zones are excluded from the analysis.

2.2 Scholte waves and leaky Rayleigh waves

In what follows, we will use picosecond acoustics to optically excite and detect acoustic waves at the interface between liquid and solid. There are two types of interface waves may propagate on a plane solid–liquid interface: the leaky Rayleigh wave and the Scholte wave [25].

Leaky Rayleigh waves propagate at a slightly higher velocity than ordinary Rayleigh waves and attenuate more with distance because their energy continuously radiates into the fluid. If the sound velocity in the liquid is less than the Rayleigh wave velocity at the solid-vacuum interface, the corresponding surface wave at the solid-liquid interface becomes leaky, as it continuously radiates compressional sound waves into the liquid.

Scholte waves at the liquid-solid interface are true interface waves. When the viscoelasticity of the liquid and solid is ignored, they do not attenuate as they propagate. In our experiment, the PTM used was silicone oil. Since the velocity of longitudinal waves in silicone oil is lower than the velocity of transverse waves in the sample, the velocity of the Scholte wave is slightly lower than the velocity of longitudinal waves in the fluid. In this case, the wave field propagates deeper in the liquid than in the solid: the Scholte wave transmits more energy in the liquid than in the solid. Therefore, Scholte waves are typically primarily located in the liquid, with a sound velocity lower than that in the liquid (see Fig. 2.3).

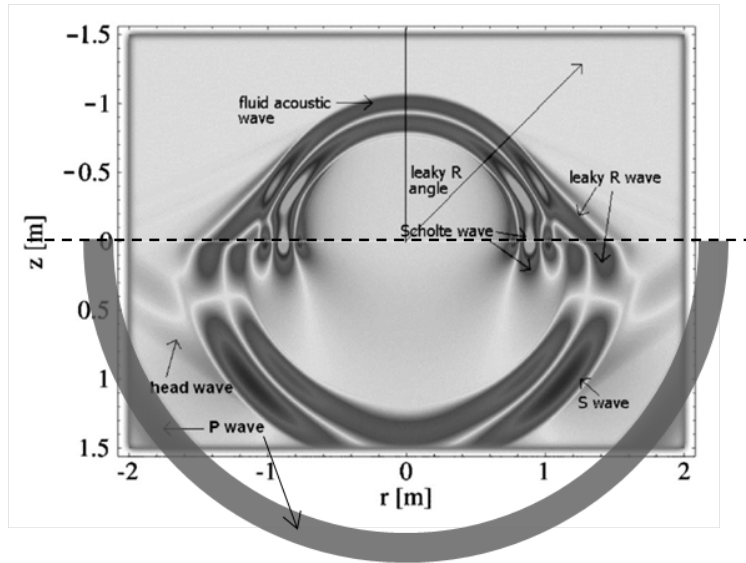


Figure 2.3: Numerical simulations obtained by the code *elastodynamic finite integration technique* (EFIT) (Fig. 4 from Zhu *et al* [25]). It shows in the sagittal plane the different kinds of waves propagating at the interface between a solid (bottom, concrete) and a liquid (top, water) submitted to a transient point load. The P-wave, originally outside the figure, has been added for better visualisation.

In the context of the dispersion equation (see Eq. (3.30) in Ref. [26]), the variable c represents the phase velocity of both Scholte and leaky Rayleigh waves, which propagate at the interface between solid and fluid media. This equation is provided as follows:

$$\left(2 - \frac{c^2}{v_T^2}\right)^2 - 4\sqrt{\left(1 - \frac{c^2}{v_L^2}\right)\left(1 - \frac{c^2}{v_T^2}\right)} - i\frac{\rho_f c^4}{\rho v_T^4} \sqrt{\frac{1 - \frac{c^2}{v_L^2}}{\frac{c^2}{v_f^2} - 1}} = 0, \quad (2.1)$$

where the parameters v_L , v_T , and v_f denote the longitudinal, transverse, and fluid wave velocities, respectively, while ρ and ρ_f represent the densities of the solid and the fluid. This equation models

two specific types of wave phenomena at the boundary between solid and fluid media: Scholte waves and leaky Rayleigh waves.

This dispersion equation yields two "physical" solutions, indicative of different types of interface waves: one is a Scholte wave, associated with a real root, characterized by its propagation along the interface without penetrating deeply into the fluid. The other is a leaky Rayleigh wave, associated with a complex root, which indicates that this wave type undergoes attenuation as it propagates, characterized by energy leakage into the fluid medium.

In our experiments, we utilized PTM, specifically silicone oil [27], which has a specific gravity of 0.95, so the density of the silicone oil is $\rho_f = 950 \text{ kg/m}^3$ ¹. For the glass, the density ρ is 2210 kg/m^3 . The longitudinal wave velocity v_L in the solid is 5618 m/s , the transverse wave velocity is $v_T = 3244 \text{ m/s}$, and the wave velocity in the fluid is $v_f = 1020 \text{ m/s}$ ². Regarding the weak viscosity of the PTM³, we assumed it to be non-viscous for the purposes of our calculations (it is likely that this assumption is not correct at the high pressures that are reached.).

The table 2.1 presents numerical solutions for the velocities of leaky Rayleigh and Scholte waves.

	solid substrate			liquid		calculations		
	v_L m/s	v_T m/s	ρ kg/m ³	v_f m/s	ρ_f kg/m ³	v_R m/s	v_{LR} m/s	v_{Sch} m/s
Glorieux <i>et al</i> (2001) [11]	glass			water		3078	$3091+i109$	1496.1
this work	cover slip glass			silicone oil		3092	$2988+i72.5$	1019

Table 2.1: Calculations of the Rayleigh wave in the solid substrate alone (v_R), leaky Rayleigh wave velocity (v_{LR}) and Scholte waves velocity (v_{Sch}), from Eq. 2.1, in two cases : glass/water (Glorieux *et al* [11]), and glass/oil (this work). i notes the imaginary number.

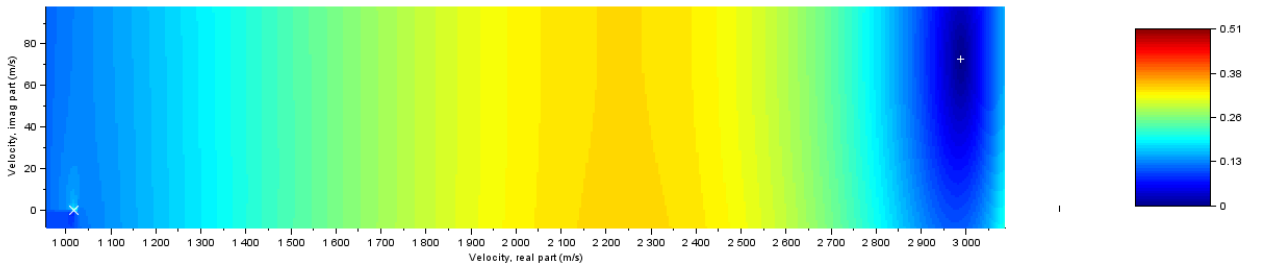


Figure 2.4: Numerical resolution of the Scholte determinant (Eq. 2.1), showing the root due to the Scholte waves (white X, at lower left) and the root due to the leaky Rayleigh wave (white +, at upper right).

The computed wave velocity of $v_{LR} = 2988+i72.5 \text{ m/s}$ represents the velocity of leaky Rayleigh waves, where the imaginary part is related to attenuation. The velocity of the Scholte appears to be slightly lower than the velocity in the fluid. For comparison, the velocity of standard Rayleigh waves is 3092 m/s .

¹See Ref. [27] p.8.

²See Ref. [27] p.18, section 13 "Sound Transmission".

³The kinematic viscosity is $\nu = 20 \times 10^{-6} \text{ m}^2/\text{s}$ at 25°C (see [27], Table p.8).

2.3 Results

2.3.1 TDBS measurements

In the glass substrate

At increasing pressure, we performed TDBS on the Al/glass side, therefore measuring the period of the Brillouin oscillations in the glass and extracting nv_L (see Fig. 2.5), where $n(P)$ is measured at $\lambda_0 = 960$ nm, and $v_L(P)$ at the frequency $f_B \simeq 10$ -20 GHz. Our data are compared with the data of Ayrinhac *et al* [18] obtained in a pure silica glass (vitreous SiO_2). We observed that as pressure increases, the longitudinal sound velocity exhibits a specific trend: initially, the velocity decreases with rising pressure, meaning there is a "softening" despite the applied high pressure, but it begins to increase once the pressure reaches approximately 2 GPa. This behavior aligns with the findings of Ayrinhac *et al* [18] in pure silica.

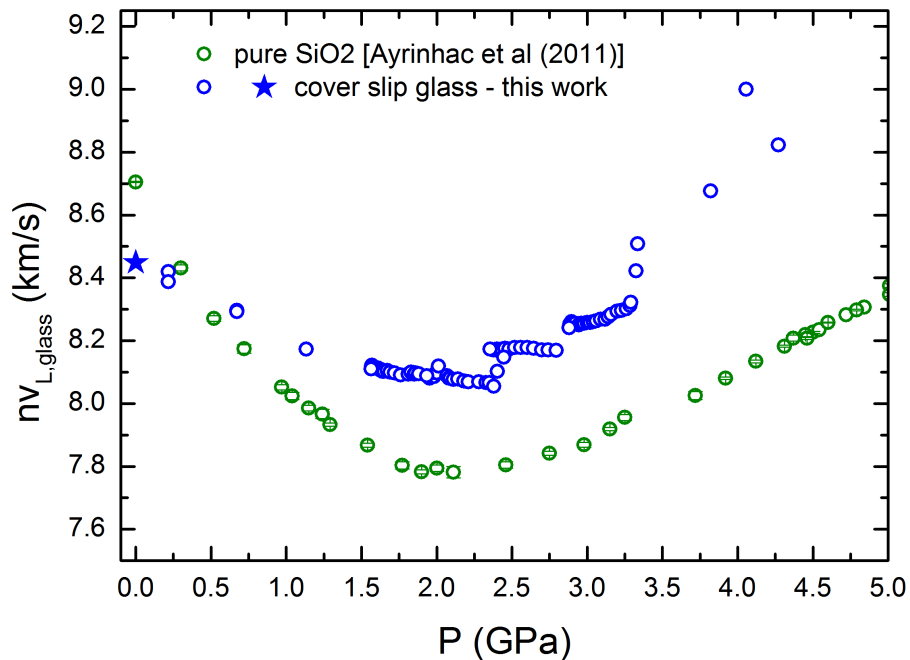


Figure 2.5: nv_L in glass, determined by TDBS at ambient pressure (blue star) and as a function of pressure (empty blue circles). The "jumps" in blue data could be attributed to variations in fine adjustments of the set-up (changes in pump and probe colinearity, position of the sample, beam focus, and so on). Our data are compared to the data of Ayrinhac *et al* (2011) [18] obtained in pure silica (SiO_2) by the Brillouin light scattering technique.

This counterintuitive phenomenon is in fact well-documented in amorphous silica (pure SiO_2) [18, 28] and more generally in glasses. The microscopic structural origin of this anomaly is still debated, with prevailing theories including local progressive transition [29] and network flexibility [30]. Additionally, and astonishingly, the elastic properties of the glass depend on the pressure-transmitting medium (PTM) [31] which can penetrate inside the voids of the glass structure. In our experiment, fortunately the PTM used (silicone oil) possesses molecules much bigger than the voids of glass network, avoiding the influence of PTM on elastic constants.

In the fluid

At decreasing pressures, we performed TDBS measurements on the Al/oil side in the compressed silicone oil (see Fig. 2.6). The spike in $nv_{L,oil}$ at around 1 GPa (dashed black box in the figure) is believed to be an anomaly, probably due to the sample being crushed between the diamonds at the final stage of the experiment. In addition, expected $nv_{L,oil}$ is added at ambient pressure (blue star) from literature data: $n(\lambda_0 = 960 \text{ nm}) = 1.3955^4$ and $v_{L,oil} = 1020 \text{ m/s}$. Our data are compared with those of Hsieh [32], and those of Wang *et al* [33]. The liquid wave velocity v_f increases greatly as a function of pressure (it increases by a factor of 5 in 4 GPa, without taking into account the potential phase transition and increase of viscosity). It seems clear that the condition $v_f < v_T < v_L$ is not fulfilled above 1 GPa (see discussion further).

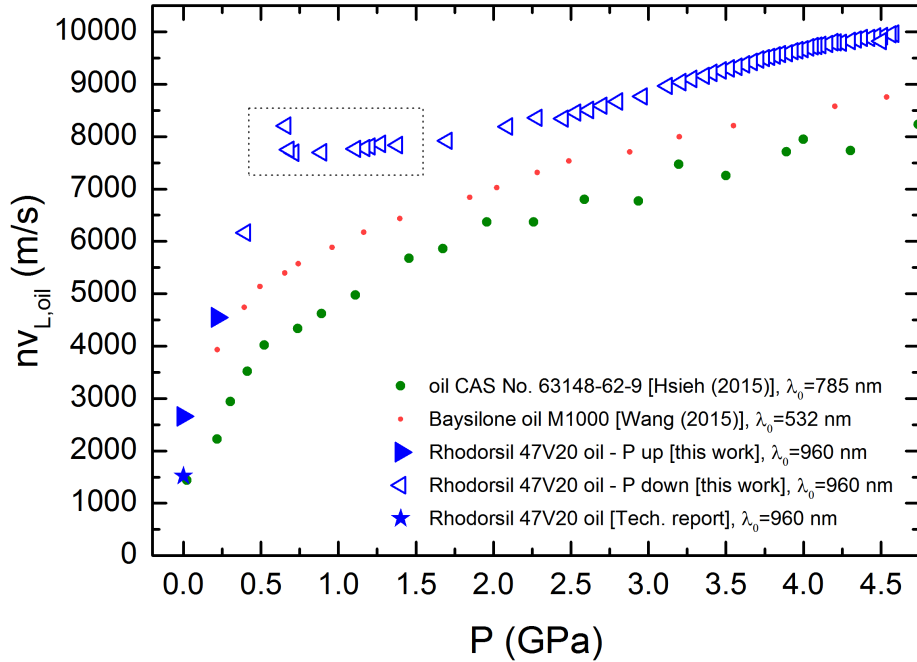


Figure 2.6: nv_L in silicone oil determined from TDBS measurements at increasing pressures (filled blue triangles), and decreasing pressures (blue empty triangles). Abnormal data points are highlighted with a dashed box. Data from this work are compared with the literature data (blue star), data from Hsieh [32] (green points) and from Wang *et al* [33] (red light points).

2.3.2 Surface imaging measurements

Velocities of surface waves

At increasing pressure, surface waves velocities were measured on the Al/glass side, meaning that the Scholte waves were not detectable. This is because theoretical considerations suggest that displacement is lower in solids than in liquids (see p. 44 in Ref. [26]). Thus, we expected to detect only two types of waves: leaky Rayleigh waves and head waves. However, surprisingly (see Fig. 2.7, left), we observed many parallel lines indicating the presence of four surface waves. In fact, it is likely due to multiple acoustic generations. From the aluminum layer, the compressional wave is reflected by an interface and returns to the aluminum, generating new leaky Rayleigh (LR) and head (H) waves

⁴Refractive index database, <https://refractiveindex.info/?shelf=organic&book=polydimethylsiloxane&page=Zhang-5-1>

approximately $\Delta t = 1.5$ ns after the initial wave generation. It produces echoes in the temporal signal (see Fig. 2.7, right).

Acoustically, there are two possibilities of the origin of this multiple generation : either the wave propagates inside the glass and is reflected at the glass/oil (or more likely glass/diamond) interface, or the wave propagates in the oil and is reflected at the oil/diamond interface.

The second case seems likely. The acoustic mismatch impedance between diamond and oil is very strong, facilitating reflection of the waves. The time interval between the two echoes is $\Delta t = 1.5$ ns. It corresponds to a distance of $d = \frac{1}{2}v_f\Delta t = 4.5$ μm , with $v_f(1.6 \text{ GPa}) \simeq 6000$ m/s. It is too short considering the difference between the thicknesses of the gasket and the sample. However, the interval of time between two laser shots is $T_{laser} = 12.494$ ns, which means that an echo appearing in the time window of the delay line could be due to a wave generated n shots earlier. Therefore, $d = \frac{1}{2}v_f(\Delta t + T_{laser}) \simeq 42$ μm and this value is compatible with the 30 μm expected (see Fig. 2.1 p.18).

However, the exact origin of this multiple generation was not elucidated.

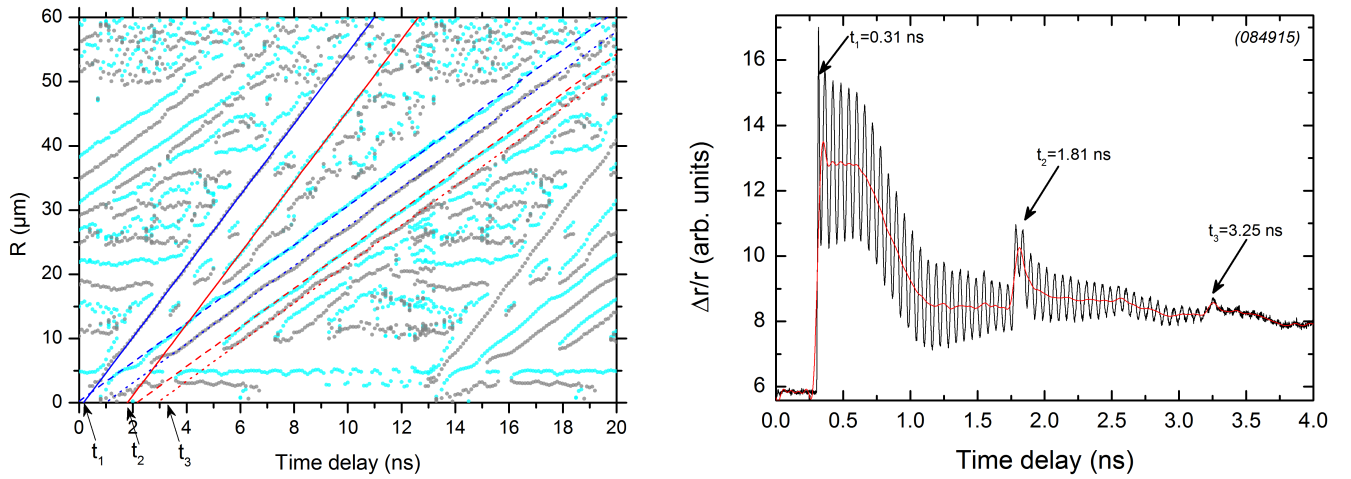


Figure 2.7: **(left)** Surface imaging obtained at 1.6 GPa, on the Al/glass side showing integrated profile as a function of time and radius (minima and maxima of the integrated profiles are shown respectively by gray points and light blue points). The multiple linear ripples correspond to surface waves : head wave (solid blue line), and leaky Rayleigh wave (dashed blue line). The identical "delayed" surface waves are shown by red lines. **(right)** Signal at $R=0$ μm (pump and probe are collinear). The echoes are shown by the arrows, once the Brillouin oscillations was removed by a smooth background (red line). The second echo arising at delay time t_3 means that it could exist surface waves generated at this time, but they are barely visible in the surface imaging.

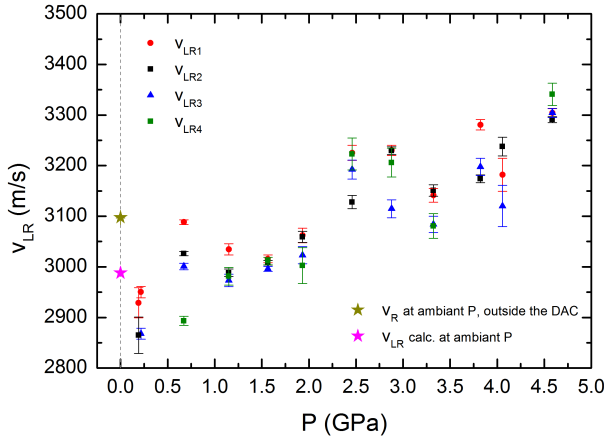
Then, the evolution of the leaky Rayleigh wave velocity and the head wave velocity as a function of pressure are shown in Fig. 2.8a and Fig. 2.8b. The multiple acoustic generation provides at most four values for v_{LR} and v_H in each movie (indicated by different symbols and colors). Reference values at ambient pressure were added (pink stars). It appears that the velocities of leaky Rayleigh waves are only increasing. The head wave initially decreases slightly with increasing pressure, then begin to increase at approximately 1.5-2 GPa. This trend is expected in glasses, as previously discussed.

However, in both parameters, v_{LR} and v_H , a "bump" can be seen at around 2.5 GPa. This "bump" is not seen in the TDBS measurements done in the glass, which indicates a probable origin in the changes of the fluid properties and a connection with the anomaly discussed previously. The fluid could be experience a phase transition (such as solidification) at this pressure. Indeed, a glass transition was detected at around 3 GPa in a PDMS oil (Baysilone oil M1000) [34]. Another explanation is brutal demixion of the oil (separation of the little polymeric chains from the bigger ones),

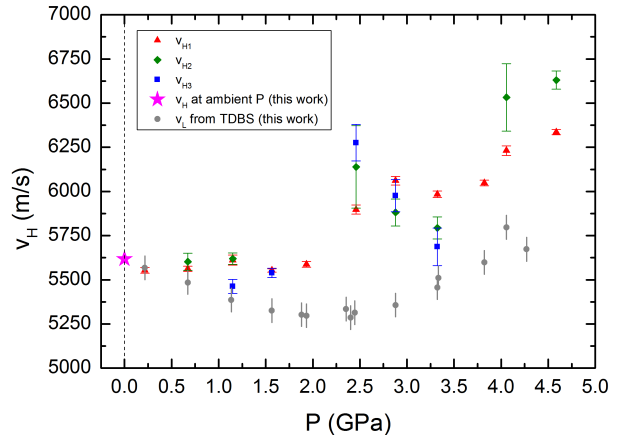
but nothing was seen optically inside the sample chamber. The jump could also be due to a purely acoustic phenomenon, as discussed in the final section (see p. 25).

We compared the head wave velocity v_H with the longitudinal velocity, v_L , obtained from TDBS measurements (see gray points in Fig. 2.8b). The value of v_L is calculated from nv_L using a simple dependence of the refractive index on pressure $n(P) = n_0 + aP$, where $n_0 = 1.504$ (see Table 1.3 p.16), and $a = 12 \pm 1 \times 10^{-3} \text{ GPa}^{-1}$ is evaluated from a silicate glass (see SAP1 in Table 1 of Ref. [35]).

It is clear from the Fig. 2.8b that v_L from TDBS does not agree with v_H , which are much higher. How can this difference be explained ?



(a) v_{LR} as a function of pressure, measured by the surface imaging method (colored different symbols). It is compared with v_R , measured at ambient conditions and outside the DAC (yellow star), and v_{LR} determined by calculations (see Table 2.1 p. 20). As discussed in the text, the exact nature of the wave at high pressure was not elucidated (Leaky Rayleigh wave or Stoneley wave).



(b) v_H as a function of pressure (colored different symbols), and at ambient pressure outside the DAC (pink star) measured by the surface imaging method, and compared with TDBS measurements (gray points).

Figure 2.8

It is clear that the sound velocity in the silicone oil increases significantly : at 5 GPa, the sound velocity in the oil is of the same order of magnitude as the sound velocity in the glass. This high value could indicate the solidification of the oil, likely experiencing a glass transition. Thus, the experiment evolves from a "hard solid-fluid" system ($v_f < v_T < v_L$) [11] at around 1 GPa, to a "soft solid-fluid" system ($v_T < v_f < v_L$) at around 2-3 GPa. In this case, Glorieux *et al* [11], demonstrated that the observed leaky Rayleigh wave have a velocity which corresponds to the longitudinal velocity in the fluid. At higher pressures, a "solid-solid" system should be considered. The measured v_H indicates a possible mixing of velocities between $v_{L, \text{glass}}$ and $v_{L, \text{solid oil}}$. At a solid-solid interface, a new kind of wave exists (Stoneley wave), and its existence and properties depends on certain elastic conditions of the two materials and if the interface is welded or slipping [36]. It could be possible to relate the v_{LR} to v_T in glass, but it needs further studies. As a conclusion, simply stated, the accurate determination of the shear velocity from surface waves at high pressure is very complicated by the pressure-induced changes in the PTM, as illustrated in the Fig. 2.9 with the silica/oil system, whose sound velocities are well-known.

Which PTM for future studies ?

Clearly, a softer fluid with well-known elastic properties is needed for future studies. Despite its high velocity (see Fig. 2.9, right), the freezing point of He is high (12.1 GPa) and the hydrostaticity is excellent up to 20 GPa [37] which makes it a good candidate for PTM ; however the gasket shrinkage during compression is very high. Neon seems a good candidate among others, with the lowest sound velocity, good hydrostaticity up to 15 GPa [37] and a freezing point at relatively high pressure (4.8 GPa). A disadvantage of using Ne is the significant shrinkage of the gasket during compression (although this is less than with He), and its current high cost⁵.

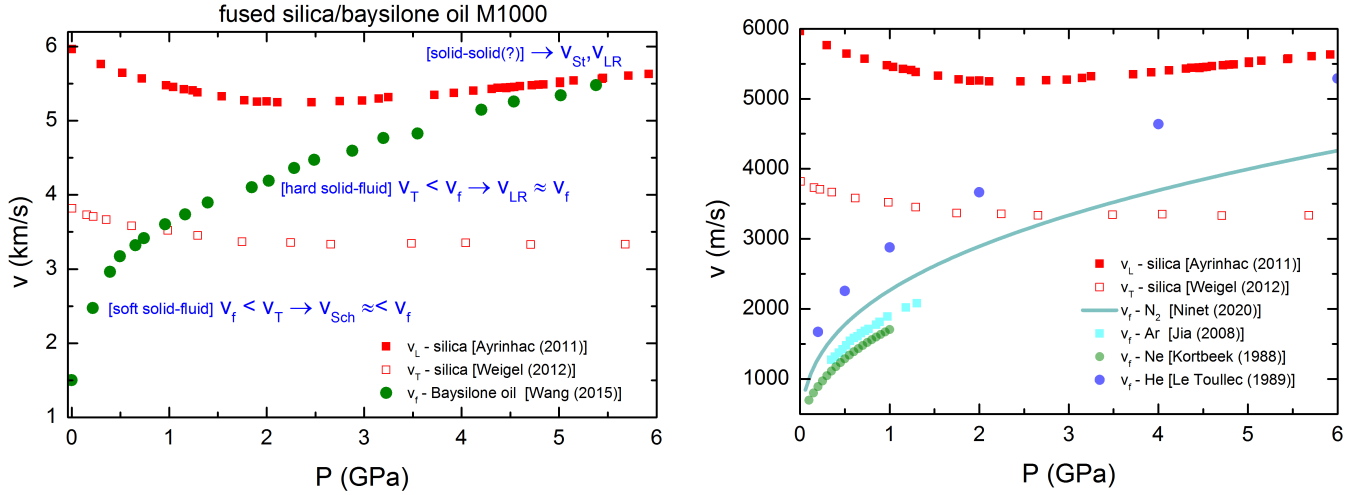


Figure 2.9: **(left)** Longitudinal and transverse velocities of fused silica (respectively filled and empty red squares) and compressional velocity of the Baysilone oil M1000 [33] (green dots) as a function of pressure. The velocity at ambient pressure is assumed to be 1.5 km/s. **(right)** Velocities of silica (red squares) and of some fluids which could be used as PTM, as a function of pressure : N₂ [Eq.(4) in [38]], Ar [Fig.(4) in [39]], Ne [Table II in [40]] and He [Table II in [40]].

To anticipate changes in sound velocities as a function of pressure, the Sholte determinant (Eq. 2.1) was solved in the case fused silica/Baysilone oil with tabulated velocities and densities (see Fig. 2.10, left). The silicone oil is assumed to be liquid at any pressure. Then, all the roots are shown in the Fig. 2.10 (right). It is clear that an abrupt transition is seen at around 1.5 GPa, which could correspond to the "bump" seen in the v_{LR} and v_H data for our studied system at around 2.5 GPa.

⁵Prices, indexed to the price of nitrogen, were as follows in september 2024 : N₂ (1), Ar (8.4), He (12.2) and Ne (506).

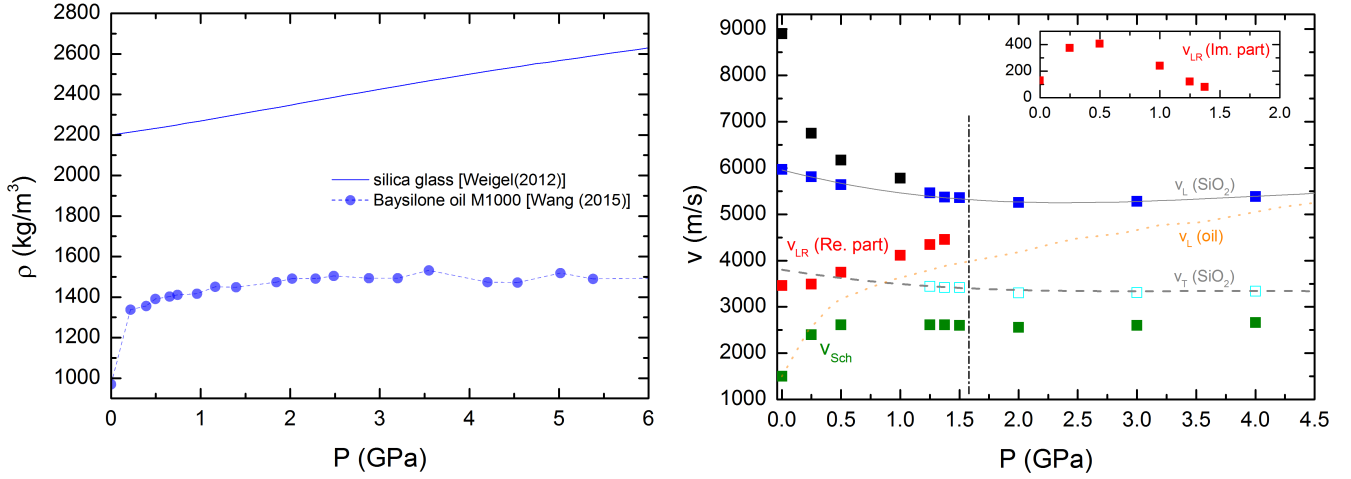


Figure 2.10: **(left)** Densities ρ of fused silica (blue line of Fig. 3 in Ref. [41]) and Baysilone oil M1000 (Eq.(5) from Ref. [33]) as a function of pressure. **(right)** Solutions of the Scholte determinant as a function of pressure, for silica/Baysilone system : real part of the leaky Rayleigh wave velocity (red squares) ; Scholte wave velocity (green squares) ; longitudinal and transverse velocity of silica (respectively continuous and dashed gray lines), and longitudinal velocity of the Baysilone oil M1000 (dotted orange line). The inset shows the imaginary part of the leaky Rayleigh wave velocity.

2.4 General conclusion and perspectives

We successfully generated and detected surface waves at high pressures on a layered sample of glass by the picosecond acoustics technique combined with a diamond anvil cell (DAC). The propagation of the surface waves was recorded using an imaging method. In addition, we performed time-domain Brillouin scattering (TDBS) measurements. The results of nv_L measured in the glass substrate are consistent with the trend of glass under high pressure, while the results measured by surface imaging are not completely consistent. We believe that this phenomenon may be caused by the solidification of the PTM under high pressure. We found that high pressure cause a large increase of sound velocity in the silicone oil, resulting in a change in the type of measured surface waves, and the interface changes from "solid-liquid" to "solid-solid", which affects our analysis of the elastic properties of the sample. It is then very complicated to obtain a accurate determination of shear waves velocity as a function of pressure.

As our experiments used standard glass, loading the sample into the diamond anvil cell is challenging and random, and the thickness of the glass prevents reaching very high pressures. PTMs also introduce some problems, such as the generation of multiple waves in the DAC sample space, which can cause waves to interfere and obfuscate the useful signal. And as we said, in our experiments, the analysis of surface waves is further complicated by the fact that the PTM solidifies gradually at around 2 GPa. To avoid the problem of solidification at low pressure, we could use a softer PTM that solidify at higher pressures, such as Ne or He, but unfortunately, sufficiently small molecules or atoms can penetrate into the glass network of the glass and significantly change its elasticity.

Despite the encouraging results obtained, the determination of the shear velocity at high pressure remains challenging. This is mainly due to the complicated sample environment in the diamond anvil cell (DAC) apparatus.

References

- [1] F Decremps, Michel Gauthier, S Ayrinhac, L Bove, Laurent Belliard, B Perrin, M Morand, Gilles Le Marchand, F Bergame, and J Philippe. Picosecond acoustics method for measuring the thermodynamical properties of solids and liquids at high pressure and high temperature. Ultrasonics, 56:129–140, 2015.
- [2] Silvia Boccato, Michel Gauthier, Nicki C Siersch, Paraskevas Parisiades, Yiuri Garino, Simon Ayrinhac, Sofia Balugani, Cécile Bretonnet, Thibault Delétang, Maëva Guillot, et al. Picosecond acoustics: a new way to access elastic properties of materials at pressure and temperature conditions of planetary interiors. Physics and Chemistry of Minerals, 49(6):20, 2022.
- [3] Sabrina Fourez, Frédéric Jenot, Mohammadi Ouafrouh, Marc Duquennoy, and Mohamed Ourak. Non-contact thickness gauging of a thin film using surface waves and a void effect on their propagation. Measurement Science and Technology, 23(8):085608, 2012.
- [4] Osamu Matsuda and Oliver B Wright. Theory of detection of shear strain pulses with laser picosecond acoustics. Analytical Sciences/Supplements, 17(0):s216–s218, 2002.
- [5] T Pezeril, P Ruello, S Gougeon, N Chigarev, D Mounier, J-M Breteau, P Picart, and V Gusev. Generation and detection of plane coherent shear picosecond acoustic pulses by lasers: Experiment and theory. Physical Review B, 75(17):174307, 2007.
- [6] Thomas Pezeril. Laser generation and detection of ultrafast shear acoustic waves in solids and liquids. Optics & Laser Technology, 83:177–188, 2016.
- [7] F Decremps, Laurent Belliard, Michel Gauthier, and Benoît Perrin. Equation of state, stability, anisotropy and nonlinear elasticity of diamond-cubic (zb) silicon by phonon imaging at high pressure. Physical Review B—Condensed Matter and Materials Physics, 82(10):104119, 2010.
- [8] PA Mante, Jean-François Robillard, and Arnaud Devos. Complete thin film mechanical characterization using picosecond ultrasonics and nanostructured transducers: experimental demonstration on sio2. Applied Physics Letters, 93(7), 2008.
- [9] F Xu, Laurent Belliard, D Fournier, Eric Charron, J-Y Duquesne, S Martin, C Secouard, and Bernard Perrin. Complete elastic characterization of lithium phosphorous oxynitride films using picosecond ultrasonics. Thin Solid Films, 548:366–370, 2013.
- [10] Ryan Canfield, Aleksandra Ziaja-Sujdak, John J Pitre, Matthew O’Donnell, Lukasz Ambrozinski, and Ivan Pelivanov. Simultaneous determination of young’s modulus and poisson’s ratio in metals from a single surface using laser-generated rayleigh and leaky surface acoustic waves. Journal of Applied Physics, 132(23), 2022.
- [11] Christ Glorieux, Kris Van de Rostyne, Keith Nelson, Weimin Gao, Walter Lauriks, and Jan Thoen. On the character of acoustic waves at the interface between hard and soft solids and liquids. The Journal of the Acoustical Society of America, 110(3):1299–1306, 2001.

- [12] Christoph T Schroeder and Waymond R Scott Jr. Finite-difference time-domain model for elastic waves in the ground. In Detection and Remediation Technologies for Mines and Minelike Targets IV, volume 3710, pages 1361–1372. SPIE, 1999.
- [13] Daniel Royer and Eugene Dieulesaint. Ondes élastiques dans les solides: propagation libre et guidée. Masson, 1996.
- [14] NK Bourne and Z Rosenberg. The dynamic response of soda-lime glass. In AIP conference proceedings, volume 370, pages 567–572. American Institute of Physics, 1996.
- [15] NK Bourne, LC Forde, JCF Millett, and JE Field. Impact and penetration of a borosilicate glass. Le Journal de Physique IV, 7(C3):C3–157, 1997.
- [16] Deep Choudhuri and Yogendra M Gupta. Shock compression and unloading response of 1050 aluminum to 70 gpa. In AIP Conference Proceedings, volume 1426, pages 755–758. American Institute of Physics, 2012.
- [17] GW Farnell and EL Adler. Elastic wave propagation in thin layers, in physical acoustics. NY: Academic, New York, pages 35–127, 1972.
- [18] Simon Ayrinhac, Benoit Ruffle, Marie Foret, H Tran, Sébastien Clément, Rémy Vialla, René Vacher, Jean-Claude Chervin, Pascal Munsch, and Alain Polian. Dynamical origin of anomalous temperature hardening of elastic modulus in vitreous silica. Physical Review B—Condensed Matter and Materials Physics, 84(2):024201, 2011.
- [19] Vitalyi E Gusev and Pascal Ruello. Advances in applications of time-domain brillouin scattering for nanoscale imaging. Applied Physics Reviews, 5(3), 2018.
- [20] Vitalyi E Gusev. Contra-intuitive features of time-domain brillouin scattering in collinear paraxial sound and light beams. Photoacoustics, 20:100205, 2020.
- [21] Oliver B. Wright, Osamu Matsuda, and Yoshihiro Sugawara. Real time imaging of surface acoustic waves on crystals and microstructures. Japanese Journal of Applied Physics, 44(6S):4292, jun 2005.
- [22] M. M. Bjornsson, A. B. Connolly, S. Mahat, B. E. Rachmilowitz, B. C. Daly, G. A. Antonelli, A. Myers, K. J. Singh, H. J. Yoo, and S. W. King. Picosecond ultrasonic study of surface acoustic waves on titanium nitride nanostructures. Journal of Applied Physics, 117(9):095305, 03 2015.
- [23] Nora Lahmiti. Measurement of thermal properties using picosecond acoustics. Master 2 internship report, Sorbonne Université, 2023.
- [24] Guoyin Shen, Yanbin Wang, Agnes Dewaele, Christine Wu, Dayne E Fratanduono, Jon Eggert, Stefan Klotz, Kamil F Dziubek, Paul Loubeyre, Oleg V Fat’yanov, et al. Toward an international practical pressure scale: A proposal for an ipps ruby gauge (ipps-ruby2020). High Pressure Research, 40(3):299–314, 2020.
- [25] Jinying Zhu, John S Popovics, and Frank Schubert. Leaky rayleigh and scholte waves at the fluid–solid interface subjected to transient point loading. The Journal of the Acoustical Society of America, 116(4):2101–2110, 2004.
- [26] Tony Valier-Brasier (Institut Jean Le Rond ∂ ’Alembert – Sorbonne Université). Ondes élastiques dans les solides isotropes [polycopié pour le master sciences pour l’ingénieur (spi)]. 2022-2023.

- [27] Rhodorsil® oils 47 technical information. Technical report, Bluestar Silicones France SAS. <https://www.silitech.ch/wp-content/uploads/2021/03/32.pdf>, Accessed september 2024.
- [28] Coralie Weigel, Marouane Mebarki, Sébastien Clément, René Vacher, Marie Foret, and Benoit Rufflé. Pressure-induced densification of vitreous silica: Insight from elastic properties. Physical Review B, 100(9):094102, 2019.
- [29] Liping Huang and John Kieffer. Amorphous-amorphous transitions in silica glass. i. reversible transitions and thermomechanical anomalies. Physical Review B—Condensed Matter and Materials Physics, 69(22):224203, 2004.
- [30] Andrew M Walker, Lucy A Sullivan, Kostya Trachenko, Richard P Bruin, Toby OH White, Martin T Dove, Richard P Tyer, Ilian T Todorov, and Stephen A Wells. The origin of the compressibility anomaly in amorphous silica: a molecular dynamics study. Journal of Physics: Condensed Matter, 19(27):275210, 2007.
- [31] Benoit Coasne, Coralie Weigel, Alain Polian, Mathieu Kint, Jérôme Rouquette, Julien Haines, Marie Foret, René Vacher, and Benoit Rufflé. Poroelastic theory applied to the adsorption-induced deformation of vitreous silica. The Journal of Physical Chemistry B, 118(49):14519–14525, 2014.
- [32] Wen-Pin Hsieh. Thermal conductivity of methanol-ethanol mixture and silicone oil at high pressures. Journal of Applied Physics, 117(23), 2015.
- [33] Xiaoxia Wang, Chen Chen, Xiaoli Huang, Jiayu Wang, Mingguang Yao, Kai Wang, Fengxian Huang, Bo Han, Qiang Zhou, and Fangfei Li. Acoustic and elastic properties of silicone oil under high pressure. RSC Advances, 5(48):38056–38060, 2015.
- [34] Xiehang Chen, Hongbo Lou, Zhidan Zeng, Benyuan Cheng, Xin Zhang, Ye Liu, Dazhe Xu, Ke Yang, and Qiaoshi Zeng. Structural transitions of 4: 1 methanol–ethanol mixture and silicone oil under high pressure. Matter and Radiation at Extremes, 6(3), 2021.
- [35] Tobias K. Bechgaard, John C. Mauro, Lynn M. Thirion, Sylwester J. Rzoska, Michal Bockowski, and Morten M. Smedskjaer. Photoelastic response of permanently densified oxide glasses. Optical Materials, 67:155–161, 2017.
- [36] Tony Valier-Brasier, Thomas Dehoux, and Bertrand Audoin. Scaled behavior of interface waves at an imperfect solid-solid interface. Journal of Applied Physics, 112(2), 2012.
- [37] S Klotz, JC Chervin, P Munsch, and Gilles Le Marchand. Hydrostatic limits of 11 pressure transmitting media. Journal of Physics D: Applied Physics, 42(7):075413, 2009.
- [38] S. Ninet, G. Weck, A. Dewaele, F. Datchi, V. M. Giordano, and P. Loubeyre. Sound velocity and refractive index of pure N₂ fluid and of equimolar N₂–CO₂ fluid mixture up to 15 GPa. The Journal of Chemical Physics, 153(11):114503, 09 2020.
- [39] Ru Jia, Fangfei Li, Min Li, Qiliang Cui, Zhi He, Liancheng Wang, Qiang Zhou, Tian Cui, Guangtian Zou, Yan Bi, Shiming Hong, and Fuqian Jing. Brillouin scattering studies of liquid argon at high temperatures and high pressures. The Journal of Chemical Physics, 129(15):154503, 10 2008.
- [40] PJ Kortbeek, SN Biswas, and JA Schouten. Measurement of the compressibility and sound velocity of neon up to 1 gpa. International Journal of Thermophysics, 9:803–812, 1988.

- [41] Coralie Weigel, Alain Polian, Mathieu Kint, Benoit Rufflé, Marie Foret, and René Vacher. Vitreous silica distends in helium gas: Acoustic versus static compressibilities. Physical Review Letters, 109(24):245504, 2012.